Controlling Interpenetration through Linker Conformation in the Modulated Synthesis of Sc Metal-Organic Frameworks

Ross J. Marshall,[a] Ciaran T. Lennon,[a] Andi Tao,[b] Hans M. Senn,[a] Claire Wilson,[a] David Fairen-Jimenez,[b*] and Ross S. Forgan[a]*

[a]*WestCHEM, School of Chemistry, University of Glasgow, University Avenue, Glasgow, G12 8QQ, UK.*
E-mail: Ross.Forgan@glasgow.ac.uk

[b]*Adsorption & Advanced Materials Laboratory, Department of Chemical Engineering & Biotechnology, University of Cambridge, Pembroke Street, Cambridge CB2 3RA, UK*
Email: df334@cambridge.ac.uk

SUPPORTING INFORMATION

Table of Contents:

S1. General Experimental Remarks

Chemicals and solvents were purchased from Alfa Aesar, Fluorochem, Tokyo Chemical Industry, Sigma-Aldrich, and VWR and used without further purification.

Powder X-Ray Diffraction (PXRD): PXRD measurements were carried out at 298 K using a PANalytical X'Pert PRO diffractometer (λ (CuKα) = 1.5405 Å) on a mounted bracket sample stage. PXRD patterns were predicted from single crystal structures using Mercury 3.9.[S1] (University of Glasgow) Pawley fitting was obtained using the Reflex tools in Materials Studio. (University of Cambridge)

Single Crystal X-Ray Diffraction (SCXRD): Data for **2**-HCl, **2-CuCl$_2$** and **3** were collected using a Rigaku AFC12 goniometer equipped with an enhanced sensitivity (HG) Saturn724+ detector mounted at the window of an FR-E+ SuperBright molybdenum rotating anode generator with VHF Varimax optics (70 μm focus) equipped with an Oxford Cryosystems cryostream device. (EPSRC UK National Crystallography Service) Data were collected using *CrystalClear*-SM Expert 3.1 b27[S2] and processed with *CrysAlis PRO* 1.171.38.41.[S3]

Thermogravimetric Analysis (TGA): Measurements were carried out using a TA Instruments Q500 Thermogravimetric Analyser. Measurements were collected from room temperature to 800 °C with a heating rate of 10 °C/min under an air atmosphere. (University of Glasgow)

Nuclear Magnetic Resonance Spectroscopy (NMR): NMR spectra were recorded on either a Bruker AVIII 400 MHz spectrometer or a Bruker AVI 500 MHz spectrometer and referenced to residual solvent peaks. (University of Glasgow)

Gas Uptake: N_2 adsorption and desorption isotherms were collected at 77 K using a Quantachrome Autosorb iQ gas sorption analyser. Samples were degassed under vacuum at 170 °C for 12 hours using the internal turbo pump. BET surface areas were calculated from the isotherms using the Micropore BET Assistant in the Quantachrome ASiQwin operating software. (University of Glasgow)

Scanning Electron Microscopy (SEM): Powder samples were deposited onto conductive carbon tabs mounted on aluminium stubs and coated with Pd for 150 seconds using a Polaron SC7640 sputter coater. The coated samples were transferred to and imaged using a Carl Zeiss Sigma Variable Pressure Analytical SEM with Oxford Microanalysis. (University of Glasgow)

GCMC simulation details: Grand canonical Monte Carlo (GCMC) simulations were employed to obtain N_2 adsorption isotherms at 77 K. These simulations were based on a model that includes Lennard-Jones (LJ) interactions for the adsorbate-adsorbate and adsorbate-adsorbent interactions. The LJ potential parameters for the framework atoms were adopted from DREIDING[S4] force field except for metal atoms, which were taken from UFF.[S5] N_2 molecules were modelled using the TraPPE force field.[S6] For the MOFs studied here, an atomistic representation was used starting from their crystallographic structures. The simulation box consisted of 4 (2×2×1) unit cells for all structures. A cutoff radius of 12.8 Å was applied to the Lennard-Jones (LJ) interactions, while the long-range electrostatic interactions were handled by the Ewald summation technique. Periodic boundary conditions were applied in all three dimensions. Peng-Robinson equation of state was used to convert the pressure to the corresponding fugacity used in the GCMC simulations. For each state point, GCMC simulations consisted 2×10^4 Monte Carlo cycles to guarantee the equilibration, followed by another 2×10^4 production cycles to calculate the ensemble averages. A cycle consists of n Monte Carlo moves; where n is equal to the number of molecules (which fluctuates during a GCMC simulation). Monte Carlo moves included in the simulations were insertion/deletion, translation and rotation of molecules with equal probabilities.

S2. Synthesis and Modulation of 1

The naming scheme and formulae of the MOFs reported in this study are summarised in Table S1 alongside a structural representation of their bridging organic ligands. The ligands used for construction of the MOFs (4,4′-biphenyldicarboxylic acid (bpdc) and 2,2′-bipyridine-5,5′-dicarboxylic acid (bpydc)) were purchased from commercial suppliers and used as received. Elemental analysis results supplied by Alfa Aesar for the scandium(III) nitrate hydrate were consistent with a tetrahydrate.

Table S1. Naming scheme and formulae of the MOFs reported during this study. The chemical structures of the ligands are given alongside their abbreviations.

Compound Name	Formula	Ligand
1	$[Sc_3O(H_2O)_2(bpdc)_3X]_n$	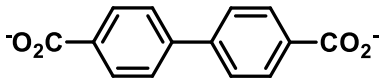 bpdc
2	$[Sc_3O(H_2O)_2(bpydc)_3X]_n$	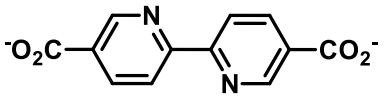 bpydc
2-$CuCl_2$	$[Sc_3O(H_2O)_2(bpydc{\cdot}CuCl_2)_3X]_n$	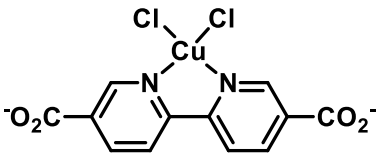 bpydc·$CuCl_2$
3	$[Sc_2(bpydc)_3]_n$	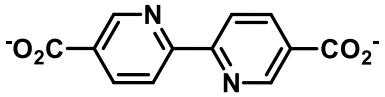 bpydc

Initial attempts to synthesise **1** were performed under a variety of conditions where the modulator was varied. Syntheses were carried out either with no modulator or with the addition of hydrochloric acid, acetic acid (AA) or L-proline. The resulting materials are herein named **1**, **1**-HCl, **1**-AA and **1**-L-proline to reflect the modulator (or lack of) added to their respective syntheses.

Synthesis and Modulation of 1

Scandium nitrate hydrate (0.085 g, 0.28 mmol, 1 eq), bpdc-H_2 (0.068 g, 0.28 mmol, 1 eq) and *N*,*N*-dimethylformamide (DMF) (6.25 ml) were added to a 25 ml PYREX reagent bottle. If required the modulator was added (Table S2), the jar was sealed and sonicated to aid homogeneous distribution of the reagents. The resulting white suspension was placed in the oven at 120 °C for 24 hours. The bottle was removed from the oven after this period and allowed to cool to room temperature. The powder was collected by centrifugation then left to stand in fresh DMF (10 ml) overnight. The product was collected by centrifugation and the DMF was exchanged for acetone. The acetone was exchanged 3 times over 3 days. The product was collected by centrifugation and placed in a vacuum desiccator to dry.

Table S2. Summary of the modulator quantities added to the synthesis of **1**.

Compound Name	Modulator	mmol	Quantity	No. of Equivalents
1-HCl	Concentrated HCl	0.28	0.025 ml	1
1-AA	Acetic Acid	8.44	0.483 ml	30
1-L-proline	L-proline	1.40	0.161 g	5

S3. PXRD Analysis of 1

PXRD patterns were collected at room temperature to determine the crystallinity and phase purity of the bulk microcrystalline MOF samples. Comparing the PXRD patterns of the modulated samples of **1** it is clear that all the materials are crystalline and their close agreement confirms their structural similarity (Figure S1).

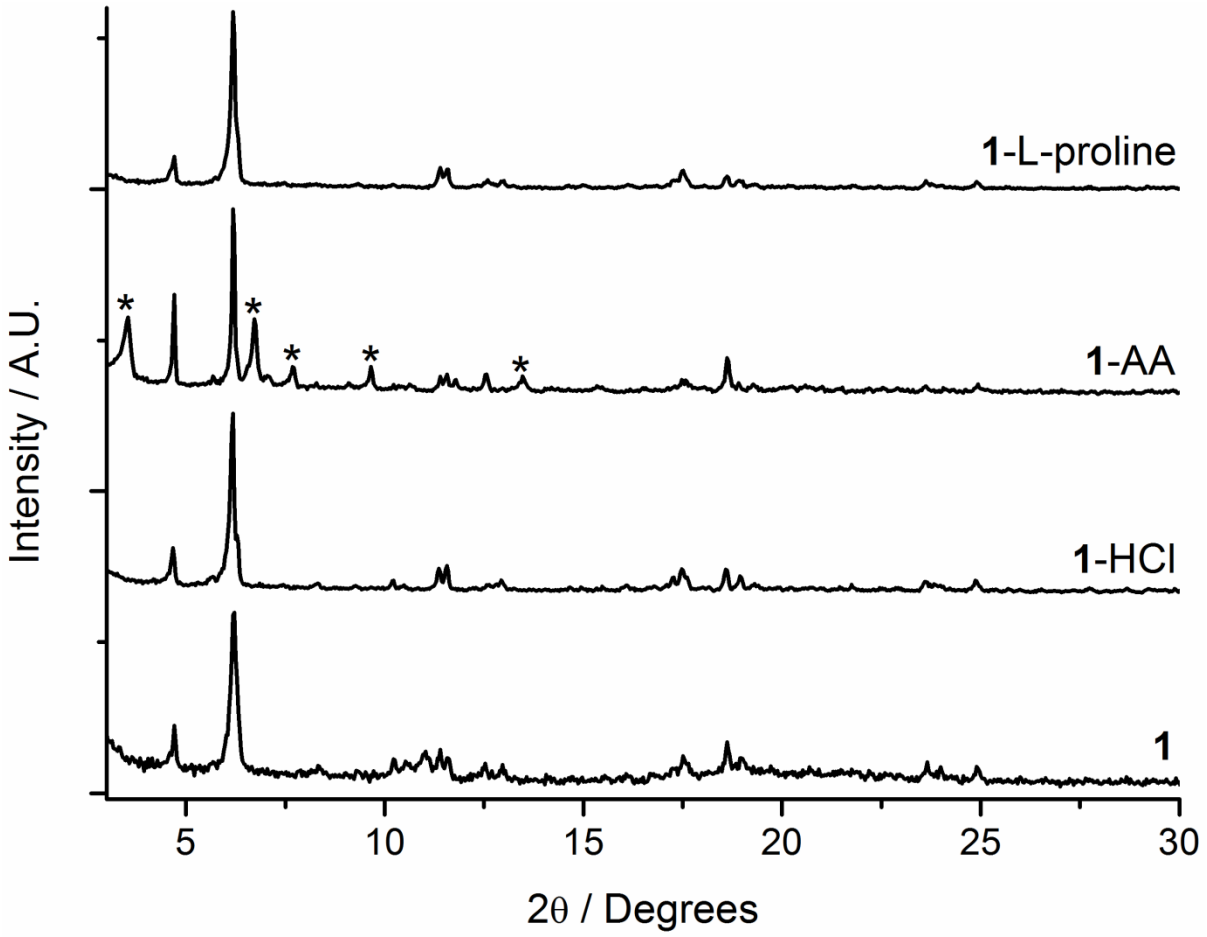

Figure S1. Stacked PXRD patterns of the samples of **1**. Additional peaks observed for **1**-AA are marked with an asterisk.

Overall there is close agreement between the PXRD patterns of the four different samples of **1** albeit there are extra peaks observed at low angles in the acetic acid modulated material (**1**-AA).

Under the conditions investigated it was not possible to isolate single crystals of **1**, however the corresponding Fe-bpdc analogue has been reported.[S7, S8] **1** is expected to be structurally analogous to the two-fold interpenetrated $[Fe_3O(H_2O)_2(bpdc)_3(OH)]_n$, more commonly known as MIL-126(Fe) (and PCN-245), and this is evident upon comparing the predicted PXRD pattern of MIL-126(Fe) (from the single crystal structure, **1**-pred) with the experimental PXRD pattern of **1**-HCl (Figure S2).

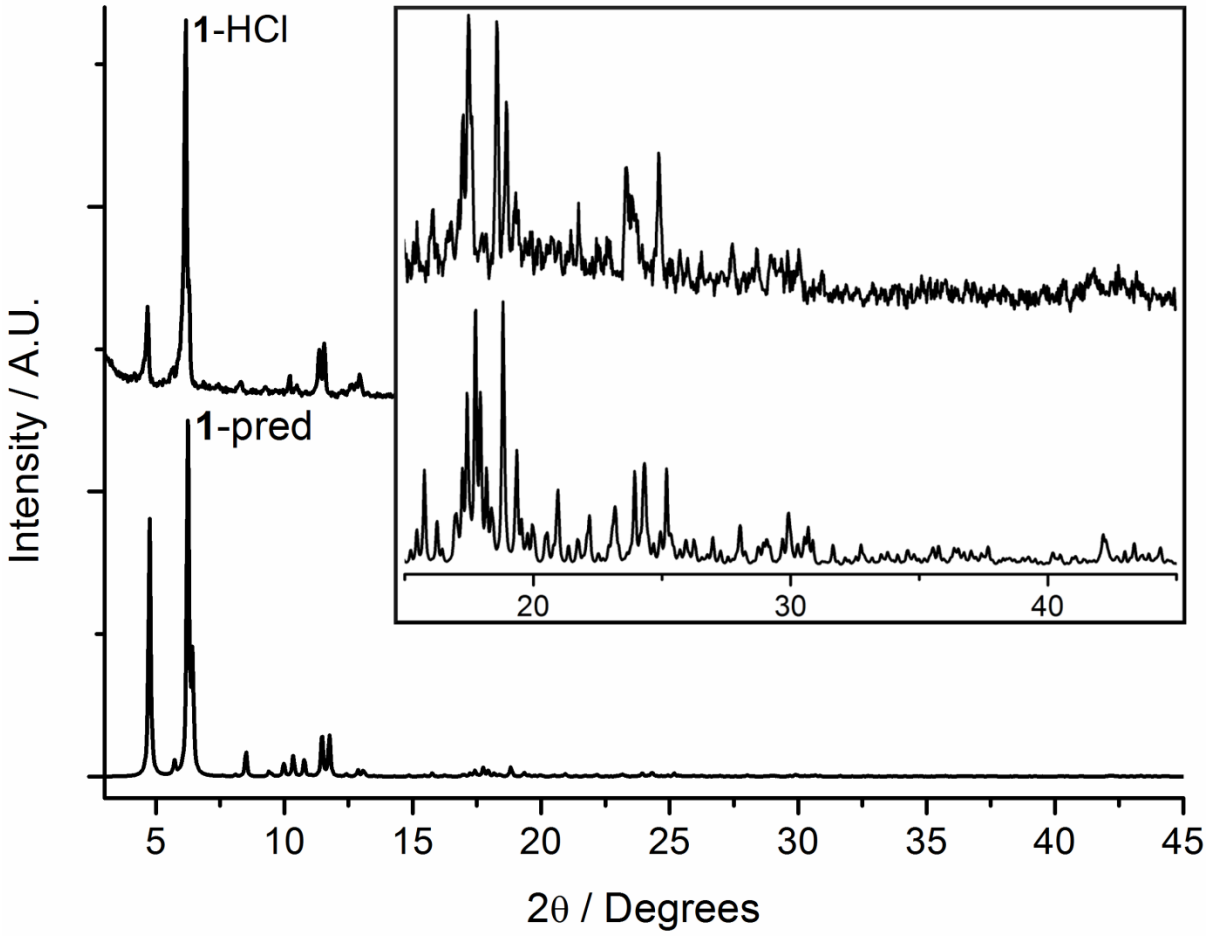

Figure S2. Comparison of the predicted PXRD pattern of MIL-126(Fe) (**1**-pred, pattern predicted from Cambridge Structural Database (CSD) Refcode MIBMER)[S7] and the experimental pattern of **1**-HCl. The inset is an expanded view of the high angle data.

The close agreement between the patterns, even to high angles of 2θ, suggests that **1** has the overall formula $[Sc_3O(H_2O)_2(bpdc)_3X]_n$ (X = OH or Cl) although this is unsurprising since Sc and Fe are well-known to form structurally identical MOFs.[S9-S11] To confirm that **1** is indeed two-fold interpenetrated, a comparison was made between the PXRD patterns of **1**-HCl and

both the predicted pattern from the crystal structure of MIL-126(Fe) and a pattern predicted from the same crystal structure but with one of the two nets removed (i.e. a non-interpenetrated structure, Figure S3).

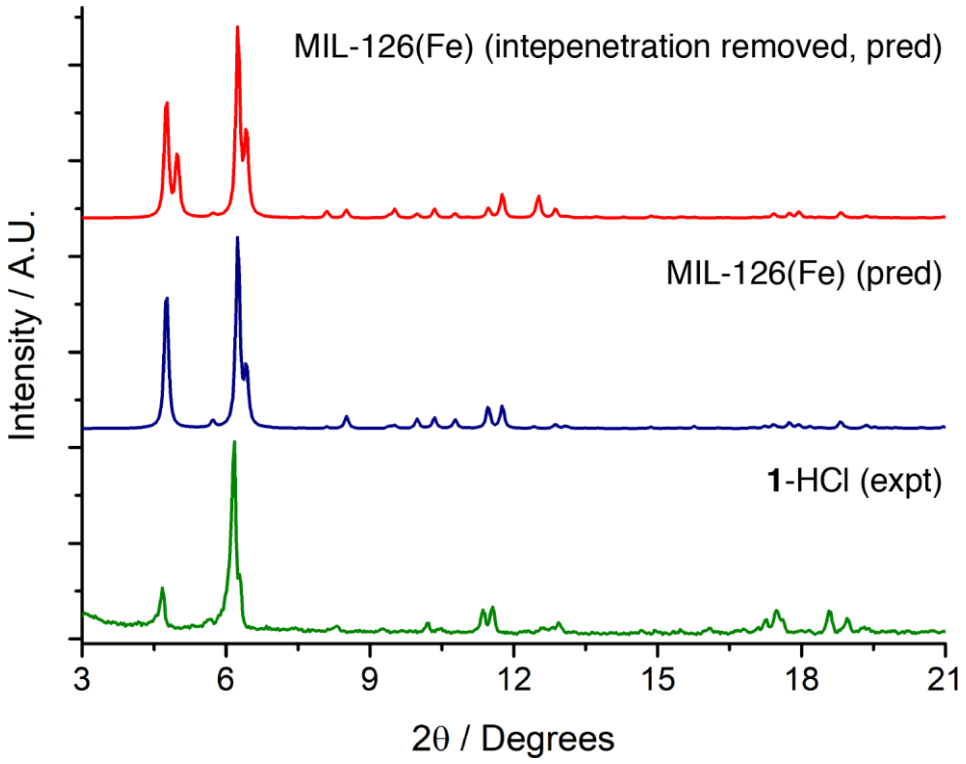

Figure S3. Comparison of the experimental PXRD pattern of **1**-HCl with patterns predicted from the crystal structure of MIL-126(Fe) and the structure generated by removing one of the interpenetrating nets (CSD Refcode MIBMER).[S7]

The comparison indicates that **1**-HCl is two-fold interpenetrated and structurally analogous to MIL-126(Fe), as the removal of one of the nets results in additional peaks in the predicted PXRD pattern which are not present in the experimental pattern of **1**-HCl; it matched much more closely to MIL-126(Fe).

To confirm the purity of the material, Pawley fitting was applied to **1**-HCl (Figure 3, main manuscript), which confirmed that the material adopts the two-fold interpenetrated, tetragonal MIL-126 structure. Therefore, **1** forms a rigid structure, and the two-fold interpenetration in **1** is expected to increase its structural stability as the increased rigidity strictly limits breathing and subsequently prevents pore collapse.

S4. Physical Properties of 1

N_2 adsorption and desorption isotherms were collected at 77 K to determine the porosity of the MOFs. The samples were activated by heating at 170 °C for 20 hours under vacuum. The two-fold interpenetration of **1** imparts suitable structural stability to allow the samples to be activated and varying levels of porosity were observed depending on the modulator added during synthesis (Figure S4).

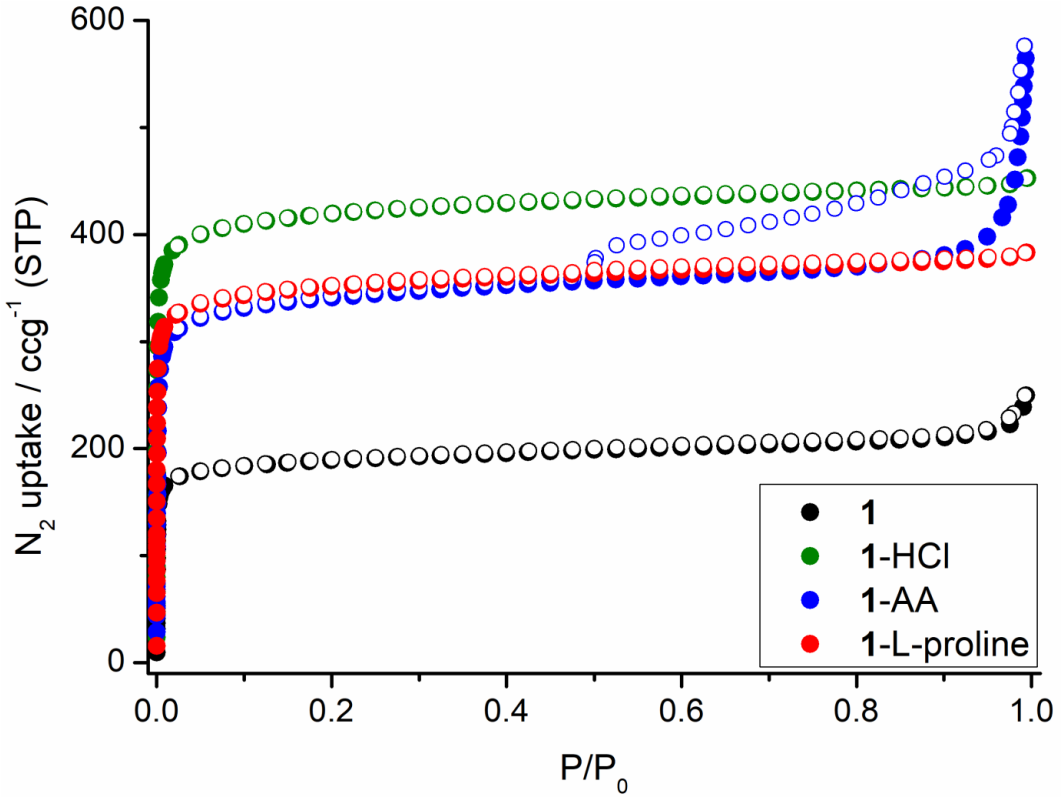

Figure S4. Comparison of the N_2 adsorption (closed circles) and desorption (open circles) isotherms (77 K) of samples of **1** synthesised in the presence of different modulators.

1, **1**-HCl and **1**-L-proline all display typical Type I isotherms with **1**-HCl being the most microporous of the samples. Surprisingly, **1**-AA displays a typical Type IV isotherm with the presence of a mesopore clearly visible. The BET areas were calculated for the four samples of **1** and are summarised in Table S3. The addition of modulators to the synthesis of **1** results in a range of BET areas, with all three modulated materials having higher surface areas than the material synthesised in the absence of a modulator.

Table S3. Comparison of the BET areas of the different samples of **1**.

MOF	BET Area (m^2g^{-1})
1	745
1-HCl	1680
1-AA	1345
1-L-proline	1405

The mesoporosity of **1**-AA is unexpected, however, an extra step is observed in its TGA profile and extra peaks are visible in its PXRD pattern, and together this suggests that the material is defective and likely contains acetate-capped Sc_3O secondary building units. Pore-size distributions were calculated (cylindrical pore, QSDFT, equilibrium model, N_2 on carbon at 77 K) for the different samples of **1** (Figure S5).

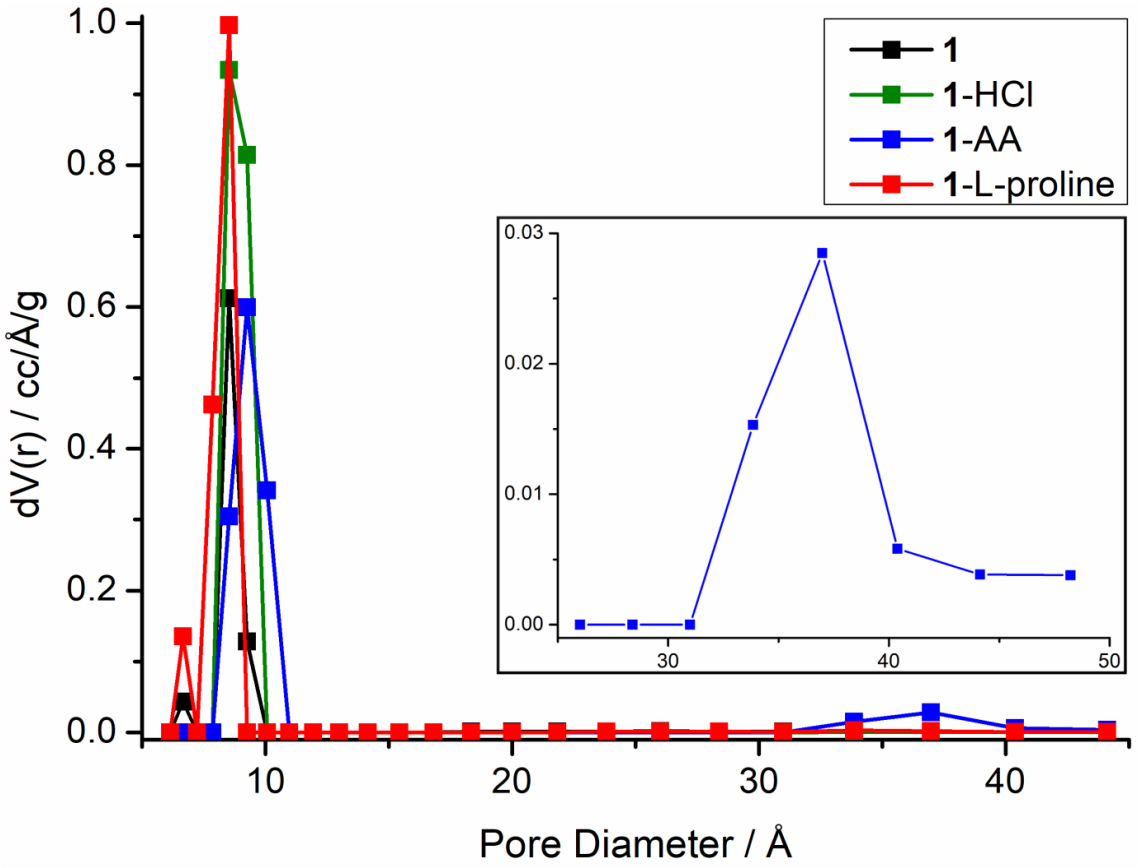

Figure S5. Comparison of the pore-size distributions of the samples of **1**. The inset is an expanded view of the mesorpore that is observed for **1**-AA.

Pore-size distribution analysis shows that the samples of **1** all contain their main pore around ~8-9 Å irrespective of the modulator used, while **1** and **1**-L-proline also contain small pores around ~6.6 Å. As expected, based on the N_2 adsorption/desorption isotherms **1**-AA contains a mesopore around 37 Å in diameter (Figure S5 inset).

To further investigate the gas uptake behaviour, grand canonical Monte Carlo simulations were used to predict N_2 uptake isotherms for **1** (assuming two-fold interpenetration) as well as a non-interpenetrated analogue. Figure S6a and S6b show the Type 1 adsorption isotherms on linear and semi-logarithmic representations, respectively. The simulated isotherm for **1** overpredicts the N_2 saturation loading measured for **1**-HCl by approximately 25%, suggesting that the porosity may not be completely activated for **1**-HCl, or the existence of amorphous non-porous phases, but crucially shows that the experimental uptake of **1**-HCl does not exceed the predicted maximum capacity of a two-fold interpenetrated structure. The simulated isotherm for the non-interpenetrated analogue of **1** shows a much larger pore volume, pore size and adsorption capacity, as would be expected (Figure S6b). It is also clear that the shape of the simulated isotherms differ in the fact that the adsorption starts at lower relative pressures for **1** compared to **1**-non-interpenetrated, suggesting that 1-HCl is indeed two-fold interpenetrated.

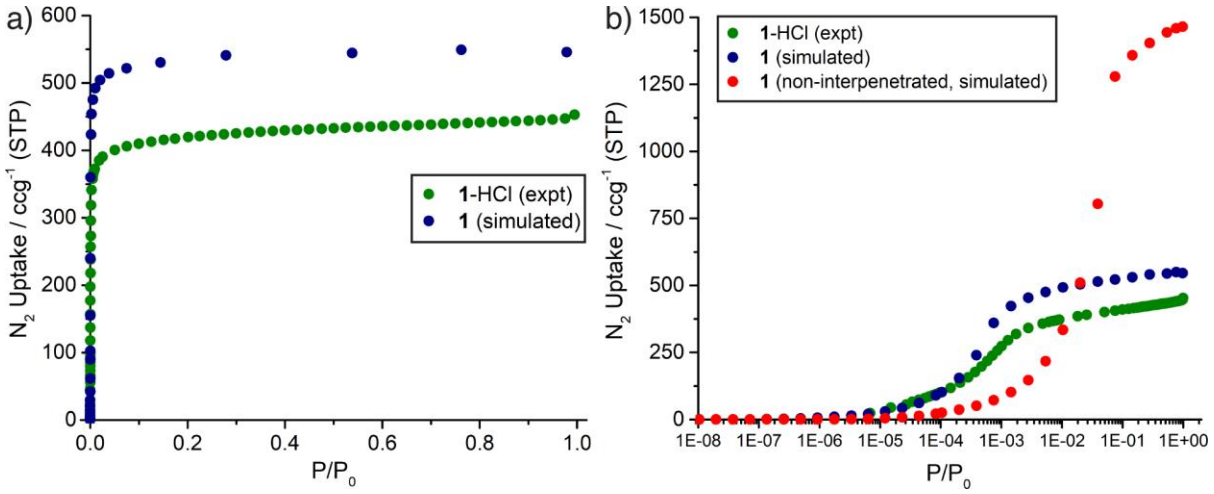

Figure S6. a) Comparison of the experimental N_2 adsorption isotherm of **1**-HCl with the GCMC simulated isotherm for **1** at 77 K. b) Comparison of the experimental N_2 adsorption isotherm of **1**-HCl with the GCMC simulated isotherm for **1**, and the structure with one net removed (i.e. non-interpenetrated) on a logarithmic scale at 77 K.

TGA profiles were collected for the MOFs by heating from room temperature to 800 °C under an air atmosphere. TGA was used to assess how the thermal stability of **1** is influenced by the addition of different modulators during synthesis (Figure S7).

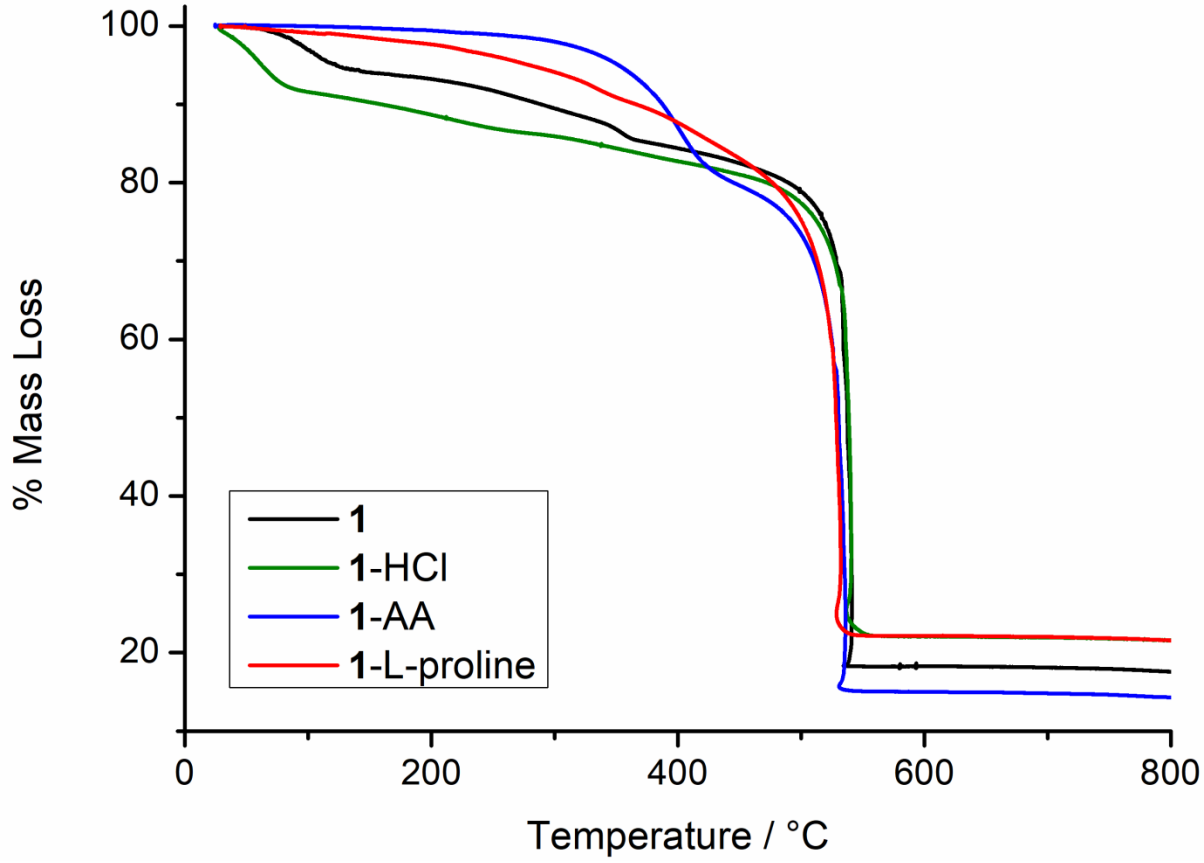

Figure S7. Comparison of the TGA profiles of samples of **1** synthesised in the presence of different modulators.

The TGA profiles reveal that the overall thermal stability is not influenced by the choice of modulator with all materials undergoing thermal decomposition at ~500 °C. There are obvious differences in the profiles of the samples below the point of thermal decomposition, although this is heavily influenced by the amount of solvent that is occluded within the pores. However, it is interesting to note that **1**-AA undergoes a significant mass loss between 300-450 °C and this mass loss presumably corresponds to the removal of residual acetate.

^{1}H NMR spectroscopy of acid digested (DMSO-d_6/D_2SO_4) samples of **1** was used to investigate the level of modulator incorporation (Figure S8).

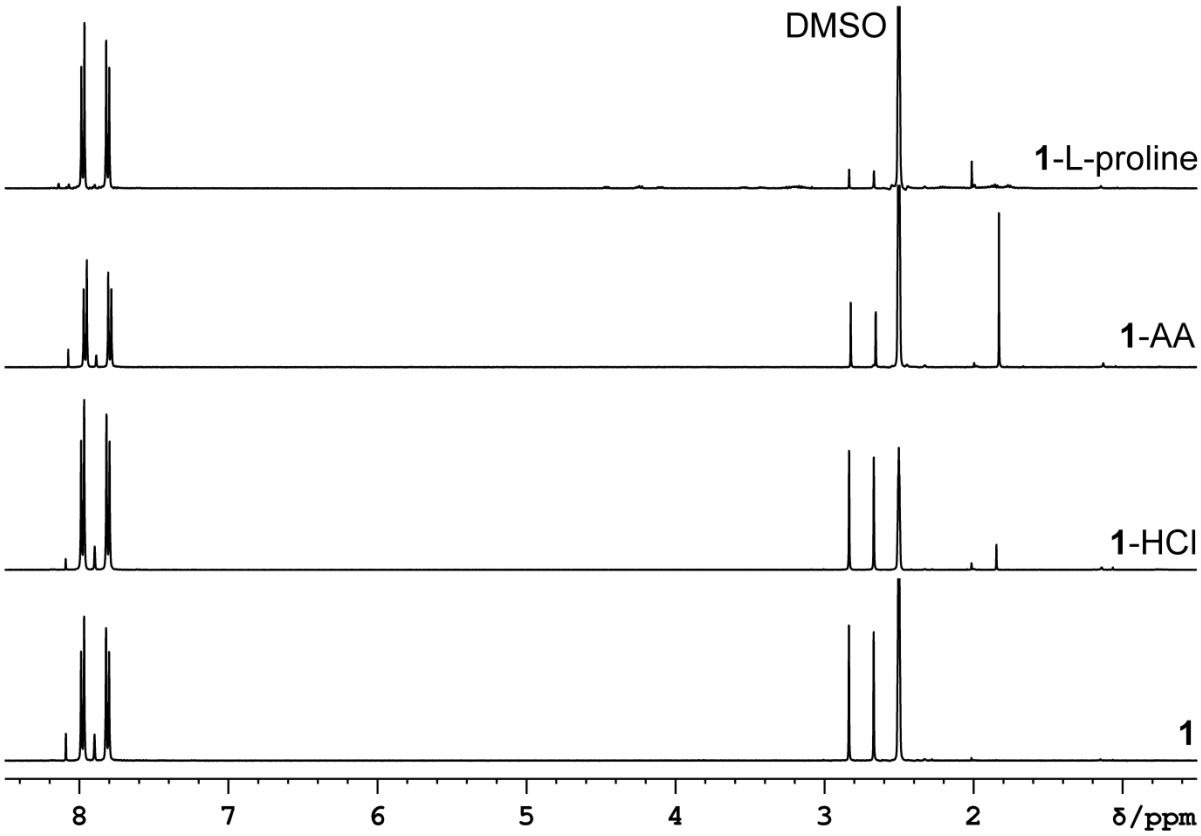

Figure S8. Stacked ^{1}H NMR spectra of acid digested (DMSO-d_6/D_2SO_4) samples of **1**, **1**-HCl, **1**-AA and **1**-L-proline.

The ^{1}H NMR spectra of the different samples of **1** are similar with varying amounts of residual DMF being the most prominent difference. In the spectrum of **1**-AA there is an extra signal observed at ~1.8 ppm and this presumably corresponds to residual acetate remaining from acetic acid added to the synthesis. ^{1}H NMR integral ratios confirm that the acetate loading is around 35 mol % compared to bpdc, suggesting that overall *ca* 15% of the bpdc ligands are replaced by capping acetates, which may explain the anomalies observed by PXRD, TGA and N_2 adsorption/desorption experiments.

1-AA was collected after N_2 sorption experiments, acid digested and analysed by ^{1}H NMR spectroscopy to determine whether the amount of acetate changed during activation (Figure S9).

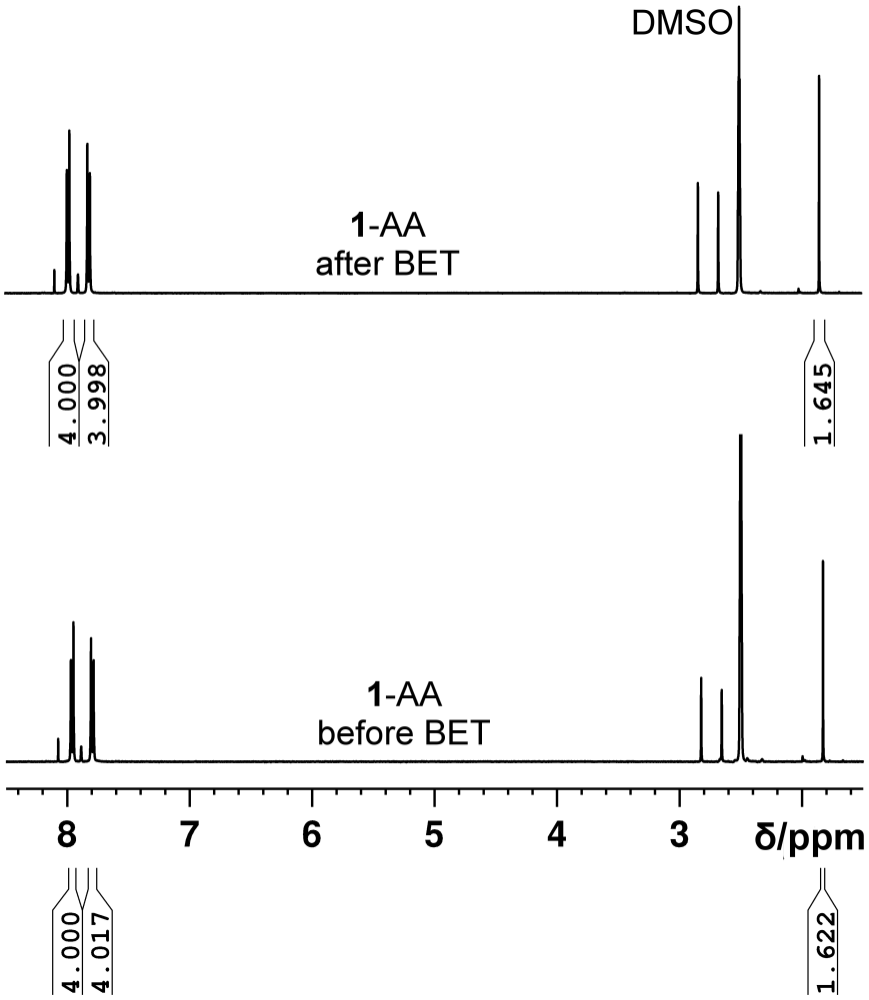

Figure S9. Stacked ^{1}H NMR spectra of **1**-AA before and after N_2 sorption experiments. The ligand protons have been integrated relative to the acetate signal to show that the acetate content remains constant.

^{1}H NMR spectroscopy unambiguously shows that the level of acetate remains constant within **1**-AA during N_2 sorption experiments and associated activation procedures (heating at 170 °C for 12 hours under vacuum). Since the acetate is not removed during activation this suggests it is either physically trapped within the MOF or that it is covalently attached. The effect of the acetic acid during synthesis is not clear; however it is evident that removal of residual acetate is not required for the creation of mesopores. As such the mesoporosity of **1**-AA is likely due to the presence of acetate capped defects.

To investigate the presence of defects in more detail, syntheses of 1 were carried out under the same conditions as in Section S2 but with different quantities of the acetic acid (AA)

modulator added. The resulting MOFs were analysed by PXRD and N_2 adsorption isotherms as shown in Figure S10.

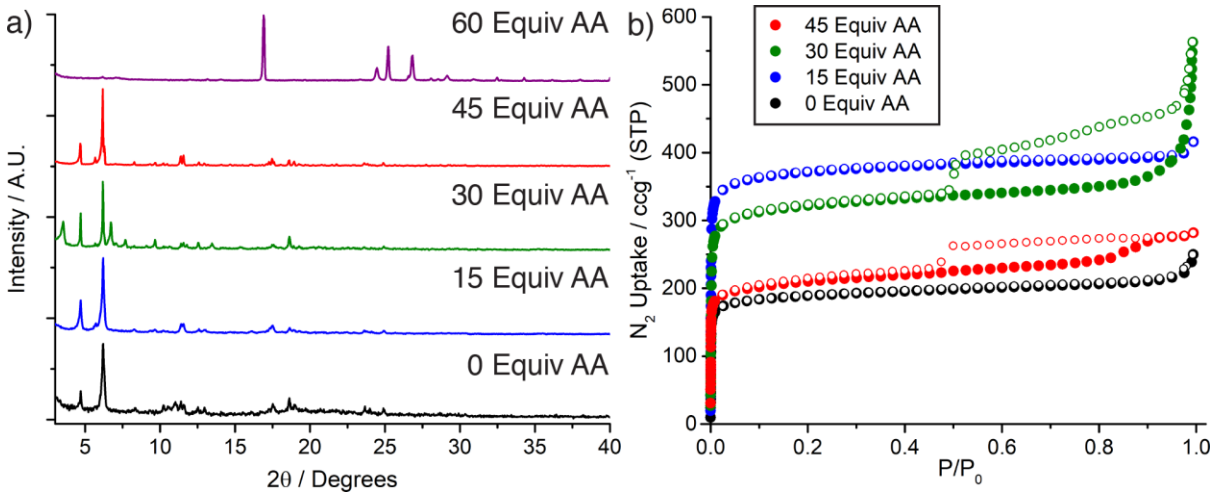

Figure S10. a) Stacked PXRD patterns of **1** modulated with differing quantities of acetic acid (AA). b) N_2 adsorption (closed circles) and desorption (open circles) isotherms (77 K) of samples of **1** modulated with differing quantities of acetic acid.

The PXRD patterns (Figure S10a) of the varying samples of **1** show that addition of AA enhances crystallinity, but in quantities greater than 45 equivalents **1** no longer forms, and presumably unreacted bpdc ligand is isolated. The N_2 adsorption isotherms (Figure S10b) show that modulation also enhances uptake, with the sample modulated by 15 equivalents of AA showing the highest uptake in the micropore region, although the mesoporosity of the sample modulated by 30 equivalents of AA leads to a higher pore volume. The mesoporosity is maintained by the sample modulated by 45 equivalents of AA but the porosity is much decreased.

S5. SEM of 1

Scanning electron microscopy (SEM) images were collected to discern the differences observed by PXRD, TGA, ^{1}H NMR spectroscopy and N_2 uptake experiments for **1**-AA compared with the other materials (Figure S11).

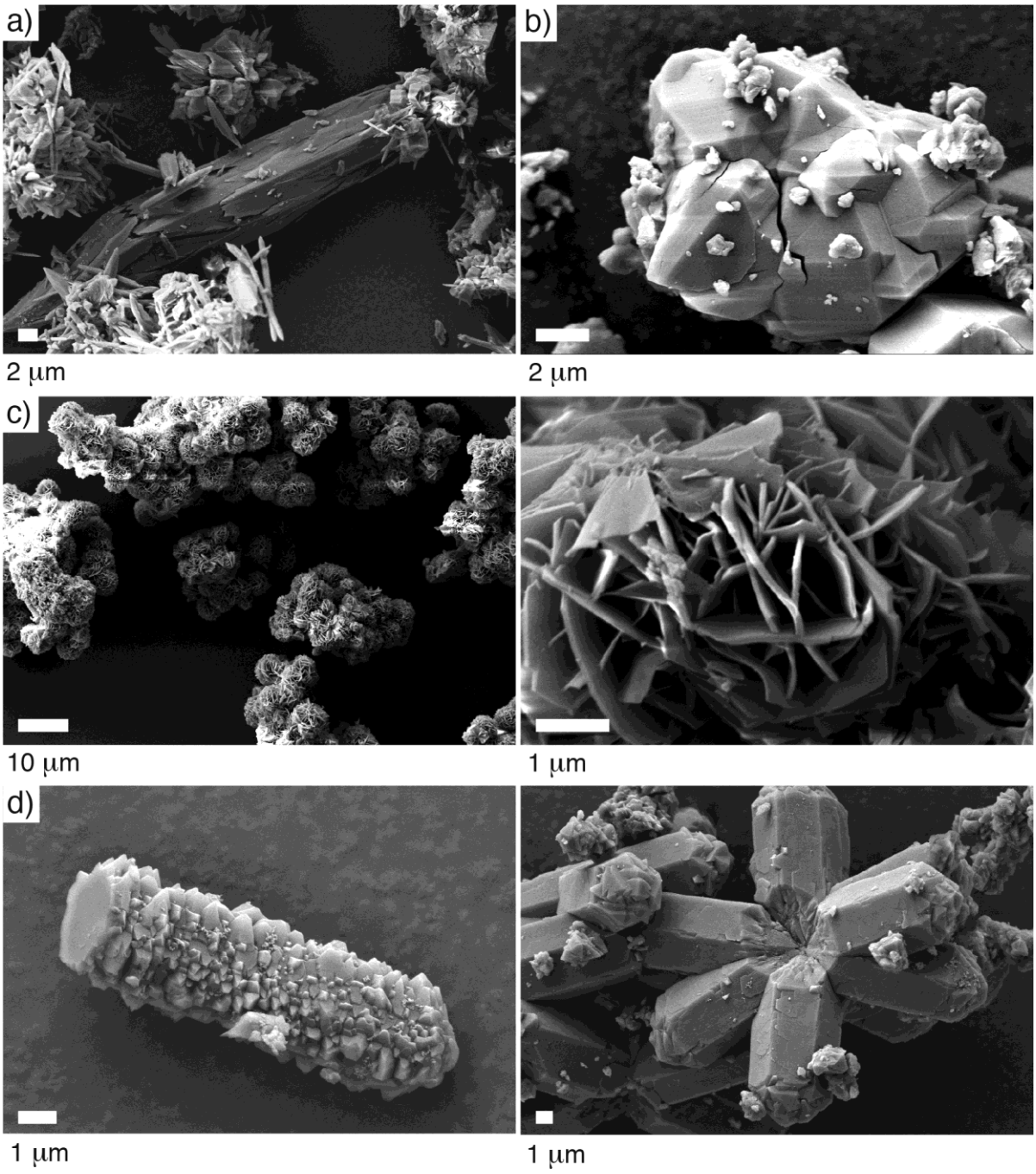

Figure S11. SEM images of a) **1**, b) **1**-HCl, c) **1**-AA (two different zoom levels) and d) **1**-L-proline (two independent regions).

SEM images of the different samples of **1** reveal that different particle morphologies are obtained in the presence of different modulators. In the absence of a modulator, lozenge shaped crystals of varying sizes result (Figure S11a), while when HCl is used larger blocky aggregates of crystals with smoother surfaces are obtained (Figure S11b). The images of **1**-AA show the most pronounced differences, with smooth plate like entities intertwining to form larger spherical aggregates (Figure S11c). Similarly, L-proline appears to induce different particle morphologies with aggregates of crystals observed to form larger hexagonal columns that further aggregate into clumps (Figure S11d). All four samples of **1** display similar PXRD patterns (Figure S1), confirming retention of the overall framework structure despite morphological changes.

S6. Synthesis of 2

Identical modulation conditions to those employed for the synthesis of **1** were used for the synthesis of **2**, however, only the HCl modulated sample (**2**-HCl) was crystalline and so HCl modulation was used for the synthesis of both bulk and single crystal samples.

Bulk 2-HCl

Scandium nitrate hydrate (0.085 g, 0.28 mmol, 1 eq), bpydc-H_2 (0.068 g, 0.28 mmol, 1 eq) and DMF (6.25 ml) were added to a 25 ml PYREX reagent bottle. HCl (0.025 ml) was added, the jar was sealed and sonicated to aid homogeneous distribution of the reagents. The resulting white suspension was placed in the oven at 120 °C for 24 hours. The bottle was removed from the oven after this period and allowed to cool to room temperature. The product was collected by centrifugation and left to stand in fresh DMF (10 ml) overnight. The product was collected by centrifugation and the DMF was exchanged for acetone. The acetone was exchanged 3 times over 3 days. The product was collected by centrifugation and placed in a vacuum desiccator to dry.

Single Crystals of 2-HCl

Single crystals of **2**-HCl were synthesised according to bulk synthesis conditions except upon cooling to room temperature the reaction DMF was exchanged for fresh DMF and the crystals were left to stand until they were analysed by SCXRD.

Crystal data for 2-HCl. $C_{36}H_{23}N_6O_{16}Sc_3$, M_r = 930.48, crystal dimensions 0.13 x 0.04 x 0.04 mm, Hexagonal, $a = b$ = 17.1503 (11) Å, c = 25.6245 (19) Å, V = 6527.2 (10) Å^3, T = 100 K, space group $P6_3/mmc$ (no. 194), Z = 2, 34005 measured reflections, 2192 unique (R_{int} = 0.172), which were used in all calculations. The final R_1 = 0.118 for 972 observed data $R[F^2 > 2\sigma(F^2)]$ and $wR(F^2)$ = 0.378 (all data). There is only one crystallographically independent terminal oxygen atom (O2) which corresponds to a H_2O for two of the three equivalent positions and an OH^- for the third. The hydrogen atoms were not located for O2 or placed in calculated positions but are included in the unit cell contents and all values derived from them. Approximately 77% of the cell volume is not occupied by the framework and contains diffuse and disordered solvent molecules. This electron density was accounted for using SQUEEZE within PLATON[S12] which calculated a solvent accessible volume of 4994 Å^3

containing 772 electrons (the equivalent of ~19 molecules of DMF) per unit cell. Crystal structure data are available from the CCDC, deposition number 1559284.

S7. Characterisation of 2

PXRD analysis of the modulated samples of **2** revealed that only the HCl modulated material (**2**-HCl) was crystalline. The PXRD patterns of **1**-HCl and **2**-HCl are compared to evaluate their structural similarities (Figure S12).

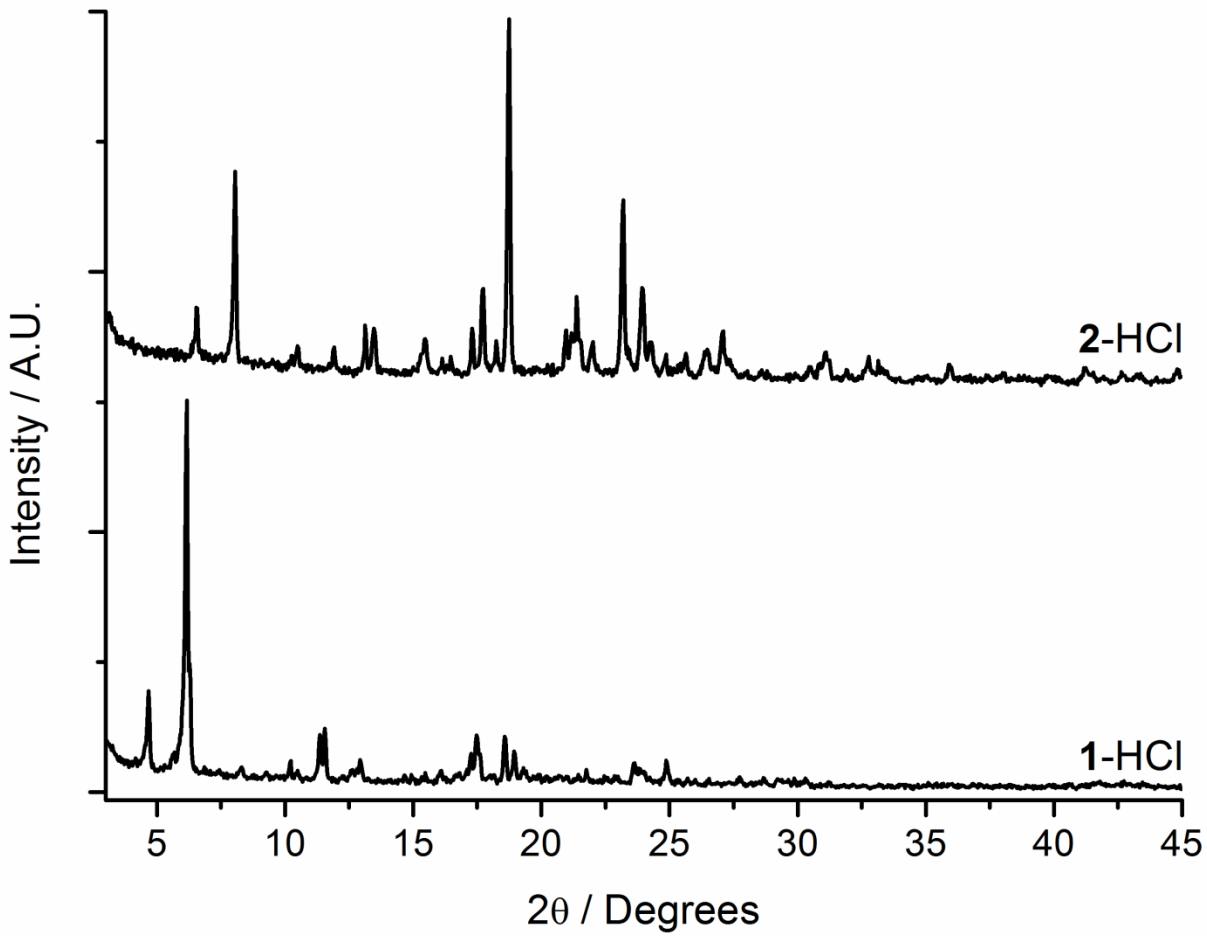

Figure S12. Comparison of the PXRD patterns of **1**-HCl and **2**-HCl.

Despite the structural closeness of the ligands the resulting MOFs do not display structural similarity with noticeable differences between their PXRD patterns. Crystals of **2**-HCl suitable for single crystal X-ray diffraction were grown, confirming that **2**-HCl adopts the MIL-88 topology with overall formula $[Sc_3O(H_2O)_2(bpydc)_3X]_n$ (where X= Cl or OH), and is not interpenetrated. MIL-88 and MIL-126 type MOFs are topologically very similar: MIL-126 is a two-fold interpenetrated derivative of MIL-88. The minor chemical differences between bpdc and bpydc (two aromatic C atoms are substituted for N atoms) appear to be

sufficient to result in Sc MOFs with differing levels of interpenetration. The PXRD pattern of **2**-HCl was predicted from its single crystal structure (**2**-pred) and compared with the experimentally obtained pattern (**2**-HCl) (Figure S13).

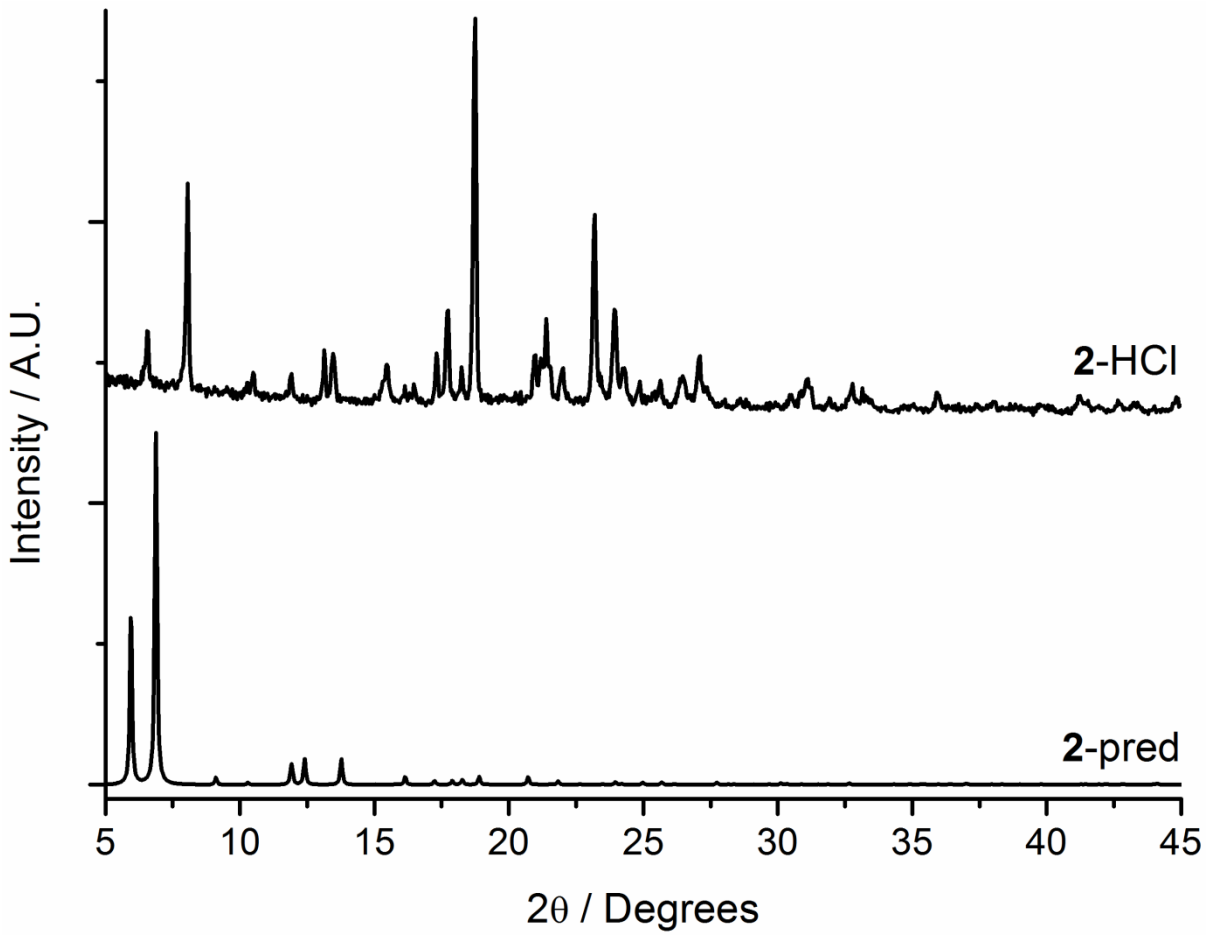

Figure S13. Comparison of the predicted and experimental PXRD patterns of **2**-HCl.

There are significant differences between the predicted and experimental PXRD patterns of **2**-HCl. Compared with the predicted pattern, in the experimental pattern major peaks move to higher angles of 2θ, indicating a decrease in unit cell dimensions during activation/drying. This is in contrast to **1** where 2-fold interpenetration increases its structural rigidity meaning that the predicted and experimental PXRD patterns are in excellent agreement (Figure S2). It is well known that flexible MOFs can transition between open pore and closed pore states (and anywhere in between)[S13] and hence the reason the predicted and experimental patterns of **2**-HCl are not in close agreement is likely due to the material adopting a closed pore form.

Pawley fitting of the PXRD pattern of **2**-HCl was attempted, but the presence of additional peaks, likely impurity phases or breakdown products, resulted in an unsatisfactory refinement (R_{wp} = 33.35%, Figure S14). The first two major peaks at low angle could correspond to a hexagonal cell (a = 15.4 Å, c = 19.3 Å) which would indicate significant contraction.

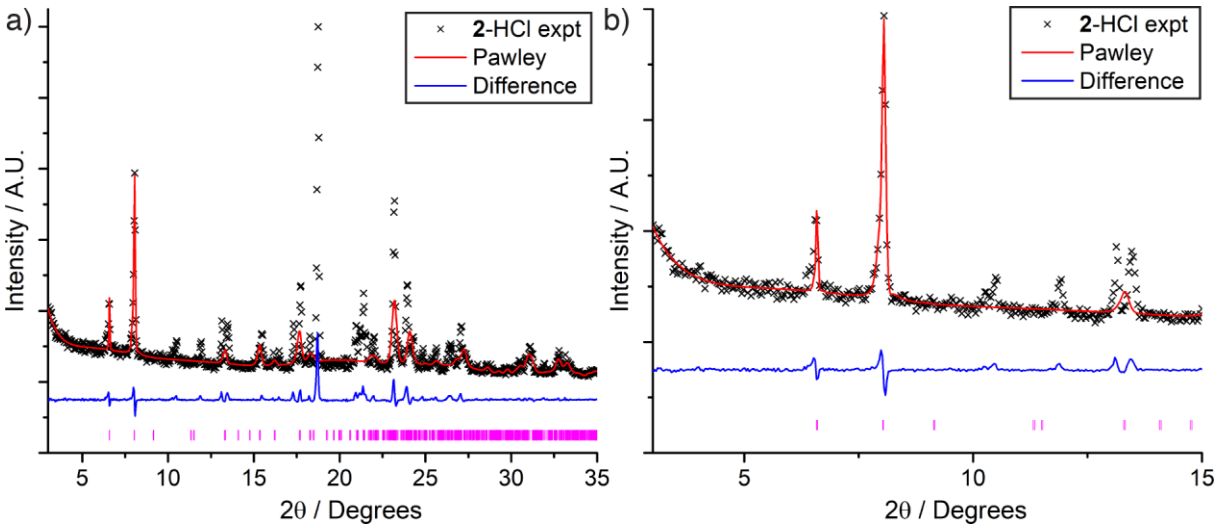

Figure S14. a) Attempted Pawley fit of the PXRD pattern for **2**-HCl. b) Zoom in of the low angle region.

SEM imaging of 2-HCl (Figure S15) showed the presence of two phases, the second was found to be a new MOF (see Section S8).

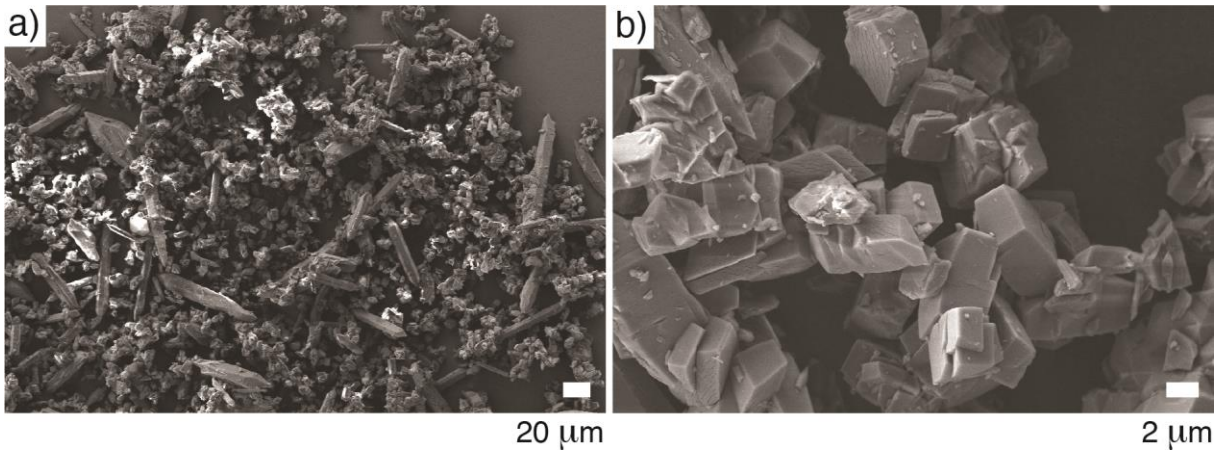

Figure S15. SEM images of a) **2**-HCl, and b) a zoomed in region with blocky crystals of a second phase distinct from **2**, which may represent **3**.

The thermal stability of the non-interpenetrated flexible **2**-HCl was also examined (Figure S16).

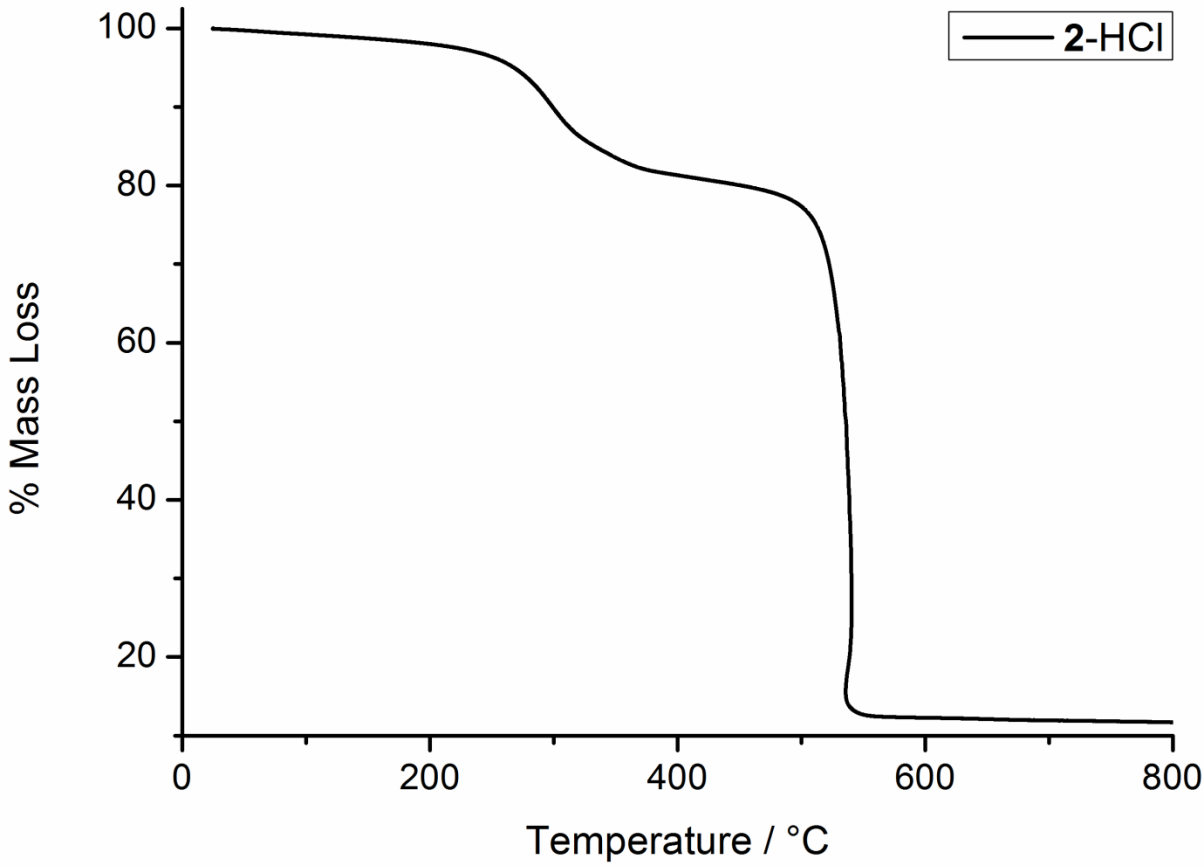

Figure S16. TGA profile of **2**-HCl.

The TGA profile of **2**-HCl reveals that after a mass loss around 300 °C it is thermally stable to ~500 °C, similar to samples of **1**. Therefore, it can be concluded that the level of interpenetration does not significantly influence the MOFs thermal stability.

N_2 uptake experiments performed on bulk samples of **2**-HCl revealed that the MOF is non-porous, further suggesting that the activated bulk powder exists in a closed pore state.

S8. Crystal Structure of 3

A single crystal of **3** was serendipitously isolated from a batch of crystals containing **2**-HCl.

Crystal data for 3. $C_{18}H_9N_3O_6Sc$, M_r = 408.24, crystal dimensions 0.13 x 0.10 x 0.05 mm, Monoclinic, a = 8.8618 (4) Å, b = 48.6247 (16) Å, c = 14.5573 (6) Å, β = 102.581 (4) °, V = 6122.1 (4) Å^3, T = 100 K, space group C_2/c (no. 15), Z = 8, 54506 measured reflections, 13433 unique (R_{int} = 0.072), which were used in all calculations. The final R_1 = 0.090 for 11018 observed data $R[F^2 > 2\sigma(F^2)]$ and $wR(F^2)$ = 0.270 (all data). The data for **3** were integrated as two equal (0.494(2)/0.586(2)) twin components corresponding to 180° about the direct lattice direction (100). The atomic displacement parameters of all the atoms of the linkers are elongated perpendicular to the plane of the rings, including the potential pivot atoms (C2/C6, C89/C12 and C14/C18) suggesting a bowing of the linker rather than twisting. There is only one crystallographically independent terminal oxygen atom (O1) which corresponds to a H_2O for two of the three equivalent positions and an OH^- for the third. The hydrogen atoms were not located for O1 or placed in calculated positions but are included in the unit cell contents and all values derived from them. Approximately 55% of the cell volume is not occupied by the framework and contains diffuse and disordered solvent molecules. This electron density was accounted for using SQUEEZE within PLATON[S12] which calculated a solvent accessible volume of 3349 Å^3 containing 1401 electrons (the equivalent of ~35 molecules of DMF) per unit cell. Crystal structure data are available from the CCDC, deposition number 1559285. The structure is shown in Figure S17.

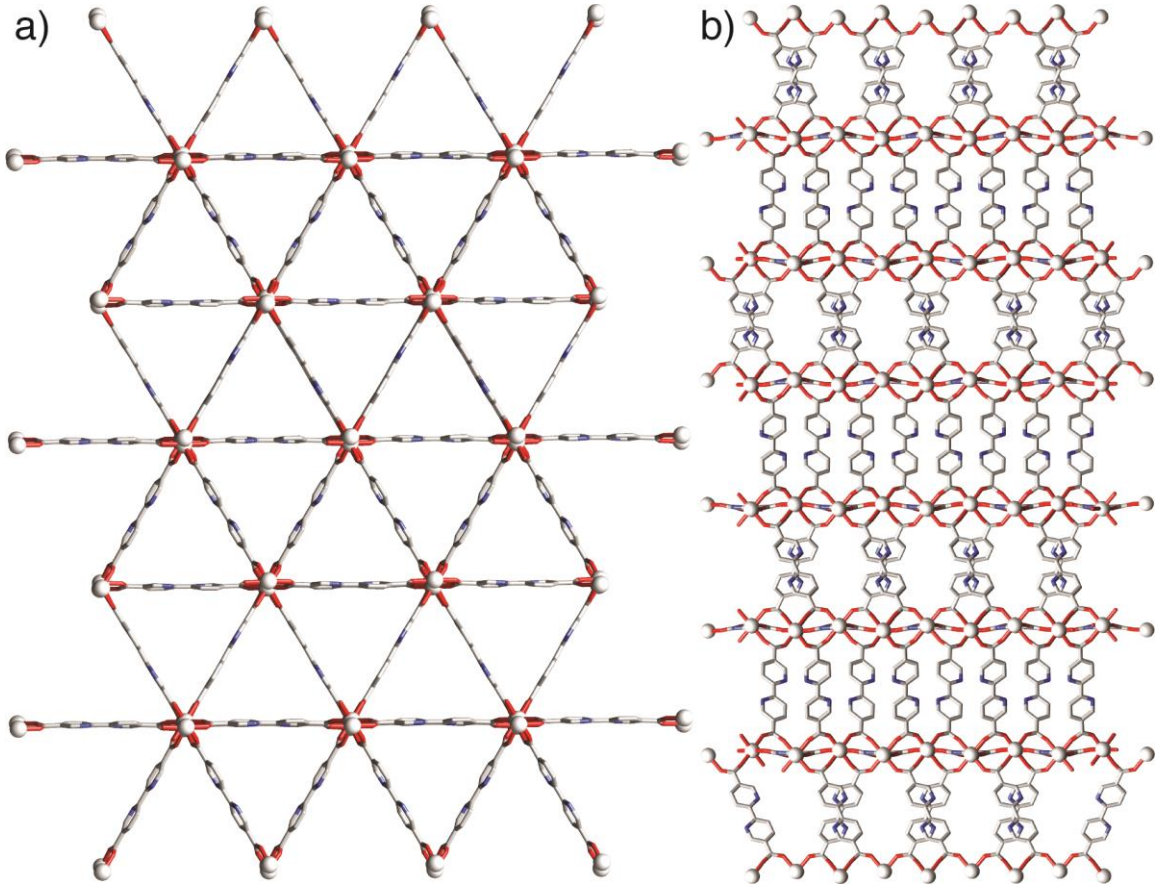

Figure S17. Portions of the solid-state structure of **3** viewed down a) the crystallographic *a* axis, and b) the crystallographic *c* axis. H atoms removed for clarity; C atoms grey, O atoms red, N atoms blue, Sc atoms silver spheres.

S9. Metallation of 2

Single Crystals of 2-$CuCl_2$

Copper(II) chloride (0.010 g, 0.07 mmol) was dissolved in anhydrous DMF (2 ml) by sonication. The solution was added to a sample vial containing single crystals of **2**-HCl in a small volume of anhydrous DMF. The vial was sealed and placed in the oven at 60 °C for 42 hours. The crystals were removed from the oven after this period and allowed to cool to room temperature. The DMF was exchanged for fresh DMF and the green crystals were left to stand until analysed by SCXRD.

Crystal data for 2-$CuCl_2$. 0.5($C_{72}H_{36}Cl_6Cu_3N_{12}O_{32}Sc_6$), M_r = 1132.14, crystal dimensions 0.15 x 0.05 x 0.05 mm, Hexagonal, $a = b$ = 17.993 (1) Å, c = 24.7387 (11) Å, V = 6936.1 (6) Å^3, T = 100 K, space group *P-62c* (no. 190), Z = 2, 55176 measured reflections, 4202 unique (R_{int} = 0.127), which were used in all calculations. The final R_1 = 0.061 for 2680 observed data $R[F^2 > 2\sigma(F^2)]$ and $wR(F^2)$ = 0.189 (all data). The symmetry of the metallated structure is much lower than that of the parent structure **2** with the Cu site ordered on one side of the linker. The space group *P-62c* (no. 190) is non-centrosymmetric and the Flack parameter is ~0.5, suggesting a racemic twin, which is not unreasonable given the centrosymmetric nature of the parent structure. Approximately 73% of the cell volume is not occupied by the framework and contains diffuse and disordered solvent molecules. This electron density was accounted for using SQUEEZE within PLATON[S12] which calculated a solvent accessible volume of 5075 Å^3 containing 1356 electrons (the equivalent of ~34 molecules of DMF) per unit cell. Crystal structure data are available from the CCDC, deposition number 1559286.

The parent and metallated structures are presented in Figure S18.

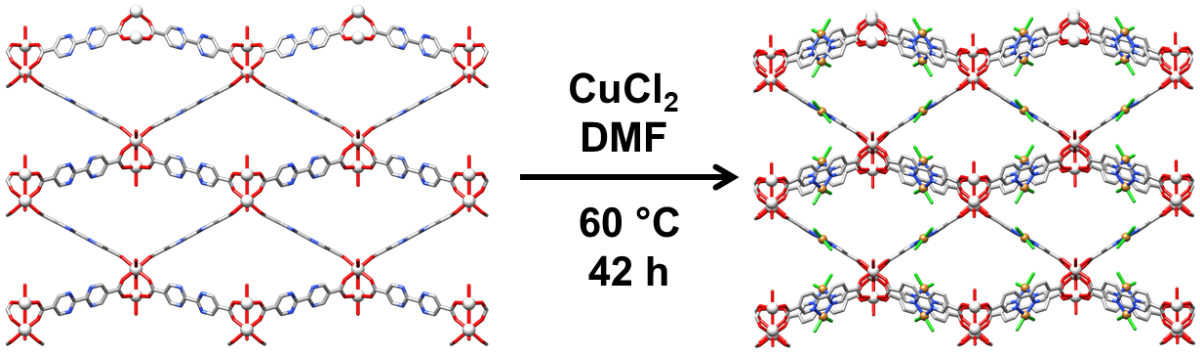

Figure S18. Comparison of the crystal structures of **2** and **2-CuCl$_2$**. H atoms removed for clarity, all partially occupied $CuCl_2$ positions displayed; C atoms grey, O atoms red, N atoms blue, Cl atoms green, Sc atoms silver spheres; Cu atoms bronze spheres.

2-CuCl$_2$ was analysed by SEM imaging to determine whether the particle morphology observed for **2**-HCl (Figure S15) could shed light on the apparent non-crystallinity of bulk samples of **2-CuCl$_2$** despite the solvated crystal structure being obtained (Figure S19).

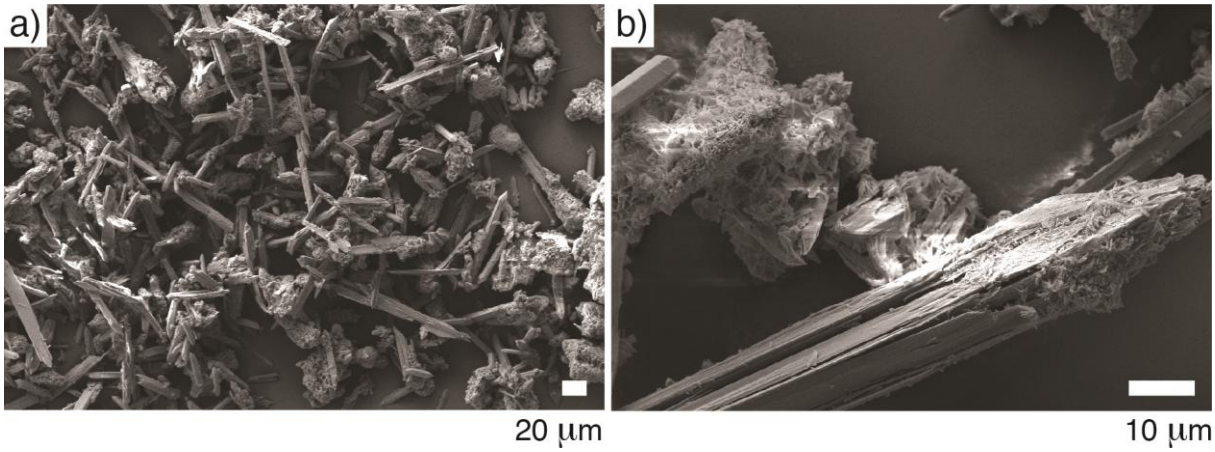

Figure S19. SEM images of two independent regions of **2-CuCl$_2$**.

Unsurprisingly the SEM images of **2-CuCl$_2$** reveal lozenge shaped crystals, similar to the parent material (Figure S16), while closer inspection of their surfaces shows that they are cracked and their ends are rough.

S10. Crystallographic Data Mining

The CSD[S14] (version 5.38, Nov 2016, including Nov 16, Feb 17 and May 17 updates) was searched using CCDC ConQuest[S15] Version 1.19 (build RC1) for the fragments in Scheme S1.

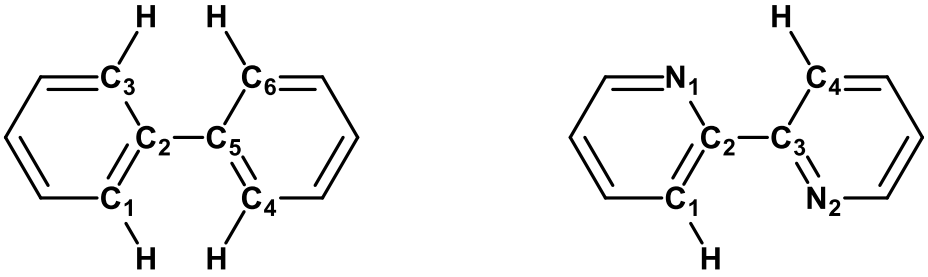

Scheme S1. Search fragments used to mine torsion angle data from the CSD. If protons are not shown on a carbon atom, then substituents were allowed.

The hits were limited to organic-only structures using the search function, to preclude structures with metals coordinated to either the nitrogen donors of the bipyridyl unit or the aromatic rings of the biphenyl units, both of which could modify the orientation of the aromatic rings with respect to each other. The four possible torsion angles around the 1–1′ bonds in the biphenyl (C_1-C_2-C_5-C_4; C_1-C_2-C_5-C_6; C_3-C_2-C_5-C_6; C_3-C_2-C_5-C_4) and bipyridyl (C_1-C_2-C_3-C_4; C_1-C_2-C_3-N_2; N_1-C_2-C_3-C_4; N_1-C_2-C_3-N_2) fragments were collected during the search, yielding 2950 hits for the biphenyl and 1243 hits for the bipyridyl fragment. The data were analysed in Mercury CSD Version 3.9[S1] (build RC1); the angles were exported, converted to absolute values, and histograms generated using Origin Pro 2016 (64 bit) Sr2 b9.3.2.303.

S11. DFT Calculations

All calculations were performed with the program Gaussian 09[S16] at the density-functional level of theory. The M06-2X exchange–correlation functional[S17] was used throughout, which yields reliable energies and structures for main-group compounds[S18, S19] and is able to account for dispersive interactions. M06-2X is a hybrid meta-GGA with 54% global exact-exchange admixture. The def2-TZVP basis set[S20] was used in all calculations. In the models of the bpdc and bpydc linkers, the metal ions coordinated by the carboxylates were modelled by sodium ions, which afforded charge-neutral models. The torsional energy profiles for rotation about the central 1–1′ bond were started from fully optimised structures of the respective molecule; the dihedral angle was scanned in 18 steps of 10°, which covers the full torsional space due to the symmetry of these molecules (Figure S20). The torsional profiles for the disodiated linkers are essentially identical to those of the unsubstituted parent molecules, biphenyl and 2,2′-bipyridine.[S21, S22]

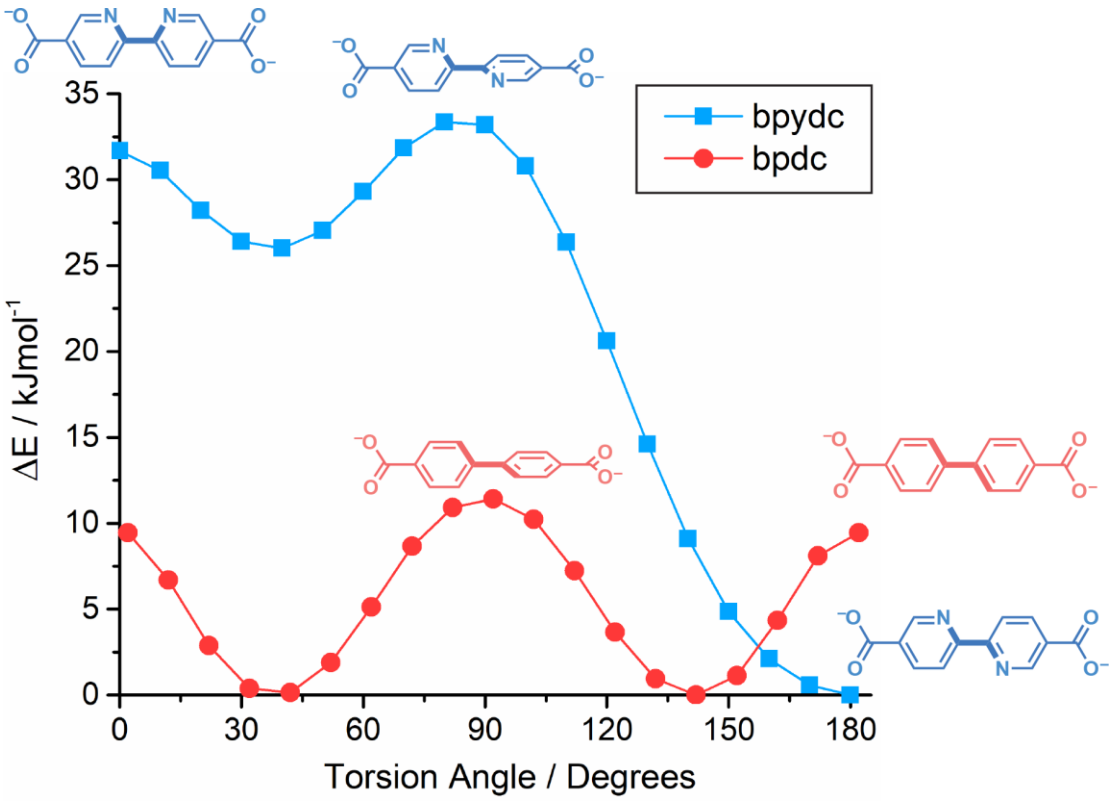

Figure S20. Calculated torsional energy profiles (M06-2X/def2-TZVP) for the disodiated linkers bpdc (red) and bpydc (blue) based on rotation of the central 1–1′ bond.

S12. References

S1. C. F. Macrae, I. J. Bruno, J. A. Chisholm, P. R. Edgington, P. McCabe, E. Pidcock, L. Rodriguez-Monge, R. Taylor, J. van de Streek and P. A. Wood, *J. Appl. Cryst.*, 2008, **41**, 466-470.

S2. Rigaku, CrystalClear-SM Expert 3.1 b27 (2012).

S3. Rigaku OD, CrysAlisPRO, UK (2015).

S4. S. L. Mayo, B. D. Olafson and W. A. Goddard, *J. Phys. Chem.*, 1990, **94**, 8897–8909.

S5. A. K. Rappe, C. J. Casewit, K. S. Colwell, W. A. Goddard III and W. M. Skiff, *J. Am. Chem. Soc.*, 1992, **114**, 10024–10035.

S6. J.J. Potoff and J. I. Siepmann, *AIChE Journal*, 2001, **47**, 1676–1682.

S7. M. Dan-Hardi, H. Chevreau, T. Devic, P. Horcajada, G. Maurin, G. Férey, D. Popov, C. Riekel, S. Wuttke, J. –C. Lavalley, A. Vimont, T. Boudewijns, D. de Vos and C. Serre, *Chem. Mater.*, 2012, **24**, 2486–2492.

S8. D. Feng, K. Wang, Z. Wei, Y. –P. Chen, C. M. Simon, R. K. Arvapally, R. L. Martin, M. Bosch, T. –F. Liu, S. Fordham, D. Yuan, M. A. Omary, M. Haranczyk, B. Smit and H. –C. Zhou, *Nat. Commun.*, 2014, **5**, 5723.

S9. J. P. S. Mowat, S. R. Miller, A. M. Z. Slawin, V. R. Seymour, S. E. Ashbrook and P. A. Wright, *Micropor. Mesopor. Mater.*, 2011, **142**, 322–333.

S10. C. Serre, F. Millange, S. Surblé and G. A. Férey, *Angew. Chem. Int. Ed.*, 2004, **43**, 6285–6829.

S11. T. Devic, P. Horcajada, C. Serre, F. Salles, G. Maurin, B. Moulin, D. Heurtaux, G. Clet, A. Vimont, J. –M. Grenèche, B. Le Ouay, F. Moreau, E. Magnier, Y. Filinchuk, J. Marrot, J. –C. Lavalley, M. Daturi and G. Férey, *J. Am. Chem. Soc.*, 2010, **132**, 1127–1136.

S12. A. L. Spek, *Acta Cryst. C* 2015, **71**, 9–18.

S13. L. Chen, J. P. S. Mowat, D. Fairen-Jimenez, C. A. Morrison, S. P. Thompson, P. A. Wright and T. Düren, *J. Am. Chem. Soc.*, 2013, **135**, 15763–15773.

S14. C. R. Groom, I. J. Bruno, M. P. Lightfoot and S. C. Ward, *Acta Cryst. B*, 2016, **72**, 171–179.

S15. I. J. Bruno, J. C. Cole, P. R. Edgington, M. Kessler, C. F. Macrae, P. McCabe, J. Pearson and R. Taylor, *Acta Cryst. B*, 2002, **58**, 389–397.

S16. M. J. Frisch *et al.*, Gaussian 09, Revision D.01., Gaussian, Inc., Wallingford, CT, (2013).
S17. Y. Zhao and D. G. Truhlar, *Theor. Chem. Acc.*, 2008, **120**, 215–241.
S18. Y. Zhao and D. G. Truhlar, *Acc. Chem. Res.*, 2008, **41**, 157–167.
S19. Y. Zhao and D. G. Truhlar, *J. Chem. Theory Comput.*, 2011, **7**, 669–676.
S20. F. Weigend and R. Ahlrichs, *Phys. Chem. Chem. Phys.*, 2005, **7**, 3297–3305.
S21. A. Göller and U. W. Grummt, *Chem. Phys. Lett.*, 2000, **321**, 399–405.
S22. I. Alkorta, J. Elguero and C. Roussel, *Comp. Theor. Chem.*, 2011, **966**, 334–339.